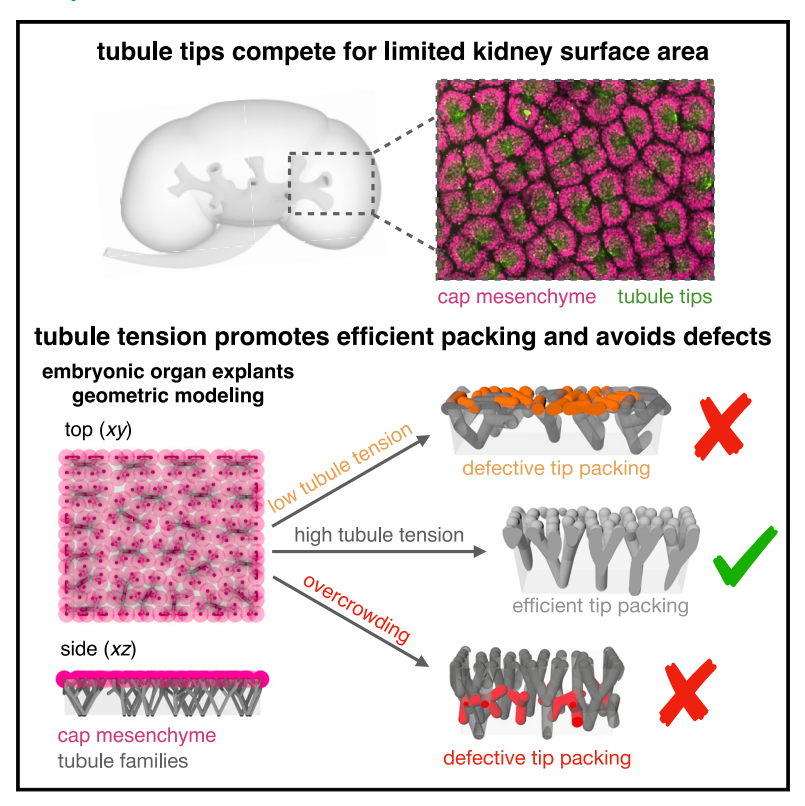
The developing murine kidney actively negotiates geometric packing conflicts to avoid defects

Graphical abstract



Authors

Louis S. Prahl, John M. Viola, Jiageng Liu, Alex J. Hughes

Correspondence

ajhughes@seas.upenn.edu

In brief

Prahl et al. show that the embryonic mouse kidney epithelium encounters a geometric packing conflict between tubule branching and available kidney surface area. Internally generated tensions reorient tubule tips to increase surface packing density and avoid defective packing outcomes.

Highlights

- Physics-based modeling maps the phase space of kidney tubule packing
- Branch nodes retract from the surface to increase packing density and avoid defects
- Actomyosin-based tubule tension is necessary and sufficient for retraction
- Removing tubule tension in dissected kidney explants causes packing defects





Article

The developing murine kidney actively negotiates geometric packing conflicts to avoid defects

Louis S. Prahl, John M. Viola, Jiageng Liu, and Alex J. Hughes 1,2,3,4,*

- ¹Department of Bioengineering, University of Pennsylvania, Philadelphia, PA 19104, USA
- ²Department of Cell & Developmental Biology, University of Pennsylvania, Philadelphia, PA 19104, USA
- ³Institute for Regenerative Medicine, University of Pennsylvania, Philadelphia, PA 19104, USA
- ⁴I ead contact

*Correspondence: ajhughes@seas.upenn.edu https://doi.org/10.1016/j.devcel.2022.12.008

SUMMARY

The physiological functions of several organs rely on branched epithelial tubule networks bearing specialized structures for secretion, gas exchange, or filtration. Little is known about conflicts in development between building enough tubules for adequate function and geometric constraints imposed by organ size. We show that the mouse embryonic kidney epithelium negotiates a physical packing conflict between increasing tubule tip numbers through branching and limited organ surface area. Through imaging of whole kidney explants, combined with computational and soft material modeling of tubule families, we identify six possible geometric packing phases, including two defective ones. Experiments in explants show that a radially oriented tension on tubule families is necessary and sufficient for them to switch to a vertical packing arrangement that increases surface tip density while avoiding defects. These results reveal developmental contingencies in response to physical limitations and create a framework for classifying congenital kidney defects.

INTRODUCTION

The metabolic costs of adult organs should make it adaptive for them to maximize their function per unit volume during development. For instance in the kidney, branching morphogenesis enables high water, ion, and macromolecule re-absorption by creating tightly packed epithelial tubules with high surface area interfaces between urine, epithelial, and endothelial layers. However, constraints and tradeoffs restrict organ function. 1-3 Currently, little is known about how development deals with geometric problems that constrain the number density of functional epithelial structures such as lung alveoli, mammary acini, or nephrons, and the ensuing total functional output of adult organs.

During the early stages of kidney development, the future urinary collecting network (ureteric bud epithelium [UB]) invades and branches into a loose connective tissue layer consisting of metanephric mesenchyme and stroma.4-6 The UB receives signaling through the glial cell-derived neurotrophic factor (GDNF)/Ret tyrosine kinase pathway, which drives initial UB invasion and subsequent branching morphogenesis. 7-9 At the same time, branching UB tips signal back to nephron progenitors in surrounding "caps" of mesenchyme to initiate nephron formation. 10,11 In the mouse, the number of daughter branches (containing tubule tips) increases from the onset of bifurcations (around E12) until branching stops at around postnatal day P2.^{12,13} The formation of the renal pelvis (a funnel-like dilation at the base of the ureteric tree) subsumes the first three or more branching generations and associated nephrons formed around embryonic day (E)12.5-E14.5.12 Since nephrons are only induced in the cap mesenchyme around UB tips, subsequent rounds of tip branching set the final number of nephrons in the adult organ such that a high tip number is likely adaptive for adult organ function. However, unlike the mammalian lung, ureteric tubule tips remain at the kidney surface throughout development. 14,15 Tip mutual avoidance/repulsion facilitates an even tip distribution at the kidney surface, potentially through exchange of repulsive paracrine factors between tips 16 or cell-cell adhesion in the surrounding mesenchyme that would form an elastic barrier resisting infiltration by neighboring tips. 17

As tips duplicate, they increasingly crowd at the surface since their number grows roughly proportional to the kidney surface area to the power 1.6 over E12-E14 and to the power 1.2 over E14-E17 (Figure S1A, inferred from data in Short et al. 12). Similar to adding more and more people to an already crowded elevator, this excess rate of tip formation creates a conflict between increasing tip number and the space available at the kidney surface. This can be resolved to a degree by shrinking the size of tubule tips and their surrounding cap mesenchyme niches as neighbors are added. 12 However, given that there must be some lower limit on niche size, any further increase in tip density could only be realized by increasing their packing efficiency (Figure S1B).18 How then does the morphology of tubule families change over developmental time to achieve this?

Advances in quantitative microscopy have created enormous insight into geometric features of UB tubule families at different



Article



stages.^{12,19-23} Although branches are globally arranged into similar clades with similar tree depths between individuals, ¹² branch point and tip spatial positions are not stereotyped.²³ In addition, genetic mutations and environmental factors including prematurity and nutrient deficiency can affect branch organization, ²⁴ kidney size, and nephron number, ²⁵⁻²⁷ and the risk of fetally programmed adult diseases. ²⁶ What principles then define tip positions at the kidney surface? Does the UB actively manage tubule organization to prevent overlapping or colliding tips?

Here, we model UB tubule organization in the developing mouse kidney. We show that geometric packing of tubule families constrained by three spatial parameters is sufficient to account for the spatial pattern of tips at the kidney surface across a large range in developmental time. Our model predicts the emergence of a frustrated tubule packing state that can either resolve through a transition to vertical packing or lead to organizational defects in which some tips collide or become buried within deeper tissue layers. We validate predicted transitions between these states using embryonic kidney explants and a soft material model of the frustrated packing state and show that a radially oriented tension along tubules is necessary and sufficient for tubule families to transition to vertical packing. Finally, we show agreement between model predictions and published tip patterns for several mutations that affect UB development. These findings suggest that UB morphogenesis actively negotiates physical packing constraints to properly organize kidney structures and avoid defects.

RESULTS

Epithelial tubule tip packing increases at the kidney surface over developmental time

Previous studies revealed that kidney branch patterns and surface tip distributions vary widely and without obvious explanation between gestational stages in mice and humans. 12,14,20 We replicated these findings by confocal immunofluorescence of mouse kidneys, which showed the characteristic E-cadherin (ECAD+)/calbindin D-28K+ branched UB with tips distributed on the surface, each surrounded by a dynamic swarm of SIX2+ cap mesenchyme cells, and separated by layers of platelet-derived growth factor receptor alpha-expressing (PDGFR α^+) stroma (Figure 1A). Tubules were organized into families in which daughter branches share a parent node, parent branches share a grandparent node, etc. We frequently observed early nephron structures interconnecting with and emanating beneath the tips (Figure 1B).

To investigate tip patterning as branching progresses, we examined the surface distribution and size of tips and cap mesenchyme clusters in whole-mount mouse kidneys at developmental stages from E14 to E18 (Figure 1C). We manually segmented tip domains (total surface area closer to a given tip than to any neighbor) and the associated "cap area" marked by SIX2 signal (Figure 1D). Tip domain area and cap area both steadily decreased throughout later developmental stages and converged after E16. The reduction in cap area is consistent with previous observations of reducing cap and tip cell numbers per domain, "12" whereas the convergence of tip domain and cap area metrics indicates closer packing of cap mesenchyme niches. This was because of a reduction in residual area occupied by stroma and parent nodes (junctions between two

daughter tips), which appeared to drop into the kidney volume more quickly after E15. Cap circularity also steadily decreased as neighboring caps encroached, causing cap shapes to conform to the area available to them. This indicates that cap domains are set by a compromise between mutual tip repulsion and confinement caused by crowding of neighboring tips over time.

Despite a lack of evidence for strict geometric control over tip positions, we reasoned that there could still be conserved "phases" of patterns with distinctive geometries and critical transitions between them, similar to other physical packing problems between mutually repulsive objects.^{28–32} For example, simulations of repulsive spheres in a 2D sheet compressed within a boundary show spontaneous ordering of the spheres and transitions between triangular, square, pentagonal "quasicrystal," or mixed packings, depending on the amount of confinement.²⁸ We observed tubule families sharing a grandparent node progressively pack into aligned regions along the surface on the scale of 3-5 families at around E15-E16 (Figures 1E and S1C). We also observed dislocations and disclinations between aligned regions, which are hallmarks of liquid crystals and elastic crystalline solids.33-35 These data and published accounts of a lack of stereotypy^{5,23} argue against a morphogenetic control program and instead for tip patterns being determined by competition between crowding and repulsion.

Geometric modeling reveals six packing phases, including defective ones

We next wondered what other such packing transitions might occur (even if not frequently observed in normal kidneys) and how to predict them. To address this, we made a computational model of tubule families governed by three spatial parameters (see STAR Methods and Figure S2): (1) the repulsion distance between tip centers, (2) the lateral domain size (width and depth) in the xy plane occupied by tubule families each sharing a greatgrandparent node, and (3) the radial height occupied by families in z (Figure 2A: Video S1). The model uses energy minimization to predict branch positions at steady state (Video S2), rather than simulating branching itself. A parameter sweep revealed six phases of tubule packing with distinct morphologies (Figures 2B and S3A), plus one trivial case where tubules are inefficiently packed (Figure S3B). Three phases are defined by parent nodes sitting near the kidney surface-"grandparent nodes at surface," "parent nodes at surface," and "H's," in the order of appearance with decreasing lateral xy domain size. The H's phase among these exhibits crystalline packing of daughter-and-parent tubule units with long-range alignment. Two defective packing states appear as the lateral xy domain size decreases from the H's phase, simulating increased tubule packing density. We call these states "short circuits" where tubules intersect near the surface and "buried tips" where surface overcrowding displaces some tips into deeper tissue layers.

Finally, a "vertical packing" phase sees tips increasing their surface packing density (Figure S3C) by reorienting to point toward the +z axis. Published examples of tip patterns qualitatively reflect increased orientational ordering of tips in *xy* between ~E13.25–E16.5, and a transition toward vertical daughter branch orientation after ~E16, in step with corresponding model cases ^{12,14,20} (Figures 2C and 2D; see Figure S2B for details on mapping kidney data to model). These data points all fell along



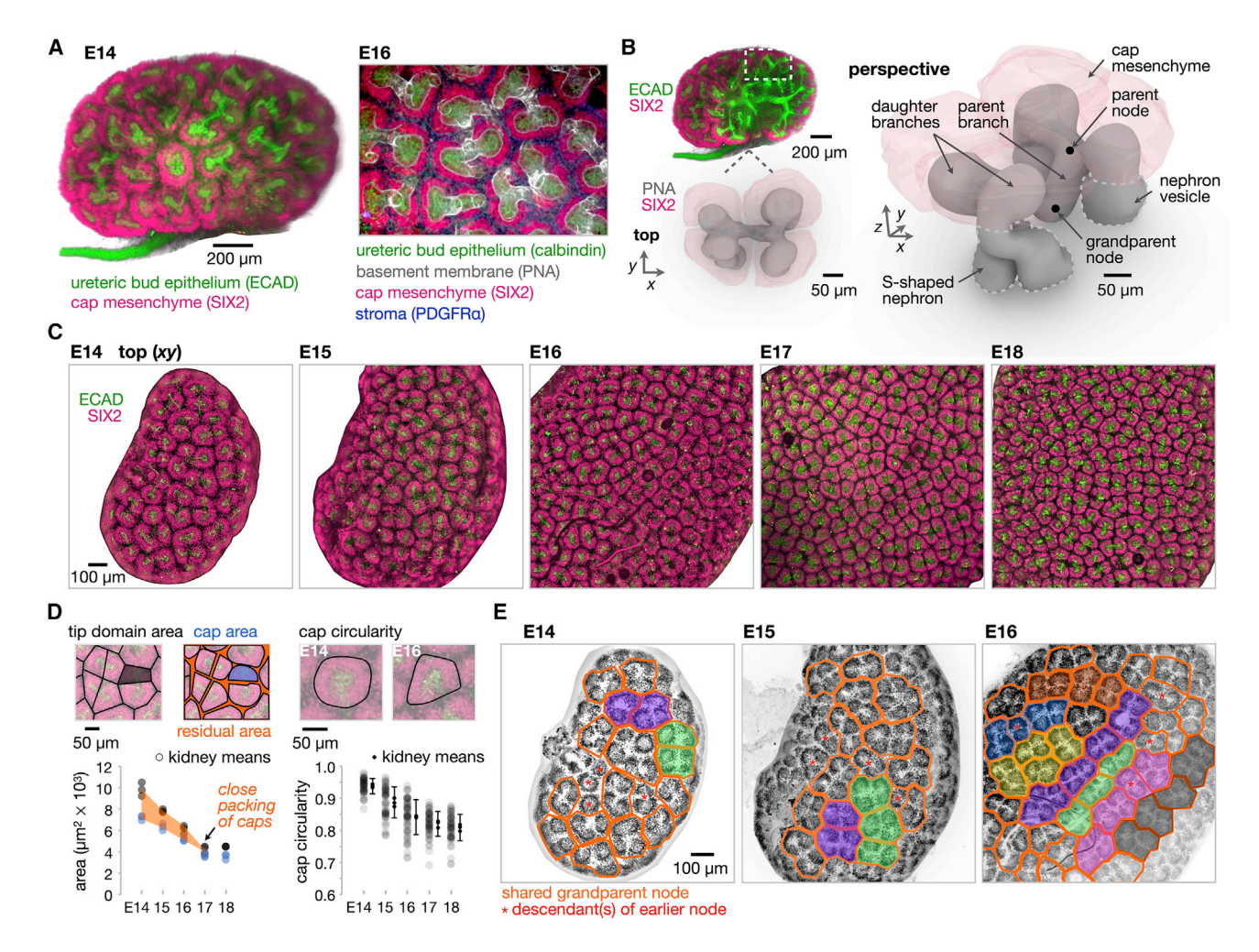


Figure 1. Ureteric bud epithelial tubule tips form diverse patterns, pack closely, and achieve long-range order

(A) Left, 10× confocal projection of cleared mouse kidney at embryonic day (E)14. Right, detail of UB tips (daughter branches) at the surface of an E16 kidney. (B) Reconstruction of tubule family sharing a grandparent node.

(D) Quantitation of: left, tip domain (total surface area per tip) and cap mesenchyme area (means of >12 measurements per n = 3 kidneys per time point); right, cap mesenchyme circularity (>18 measurements per n = 3 kidneys per time point). Error bars are mean ± standard deviation (SD) for all measurements per em-

(E) Outlines of tubule families sharing a grandparent node. Fills indicate regions of aligned families. All data are representative of two litters (biological replicates). See also Figure S1 and Table S1.

a path from the bottom-left to the top-right of the space, in other words, from parent nodes at the surface, to H's, and then to vertical tips, with none of the wild-type kidneys crossing into defective packing phases (Figure 2D; Video S3; see Figure S3 for the full list of literature cases and 2D projections of the phase space).

To assess the quantitative match between kidney data and the model, we first defined an orientational order parameter S that measures local daughter tubules alignment relative to orthogonal preferred directions (directors) when parent nodes are visible near the surface (Figure 2E; STAR Methods). S = 1 indicates crystalline packing and perfect ordering of each daughter along either director. S increased from E14 to E16 as many tubules enter the H's phase, with close agreement between experiment and model (Figure 2F). S is not defined as daughter tubules become more vertically oriented at E17-E18. We therefore also

quantified the parent branch bifurcation angle (φ) (Figures 2E and S2B) and found that this progressively decreased in both experiment and model between E14 and E18 as daughter branches shifted toward vertical packing (Figure 2F), similar to previous reports. 12,21 The model therefore captures a transition of daughter tubules from an amorphous to a crystalline H's phase at the surface at ~E16. This could be thought of as a "frustrated" state, since the model predicts that for any further increase in tip density, the H's must shift into either buried tips, short circuits, or vertical tips phases (Figure S3C).

Actomyosin-based tension on tubule families is necessary and sufficient to drive vertical packing

We next asked whether physical forces could mediate the switch to vertical packing, since this requires that parent through

⁽C) 10× projections of kidneys at fixed zoom.

Article



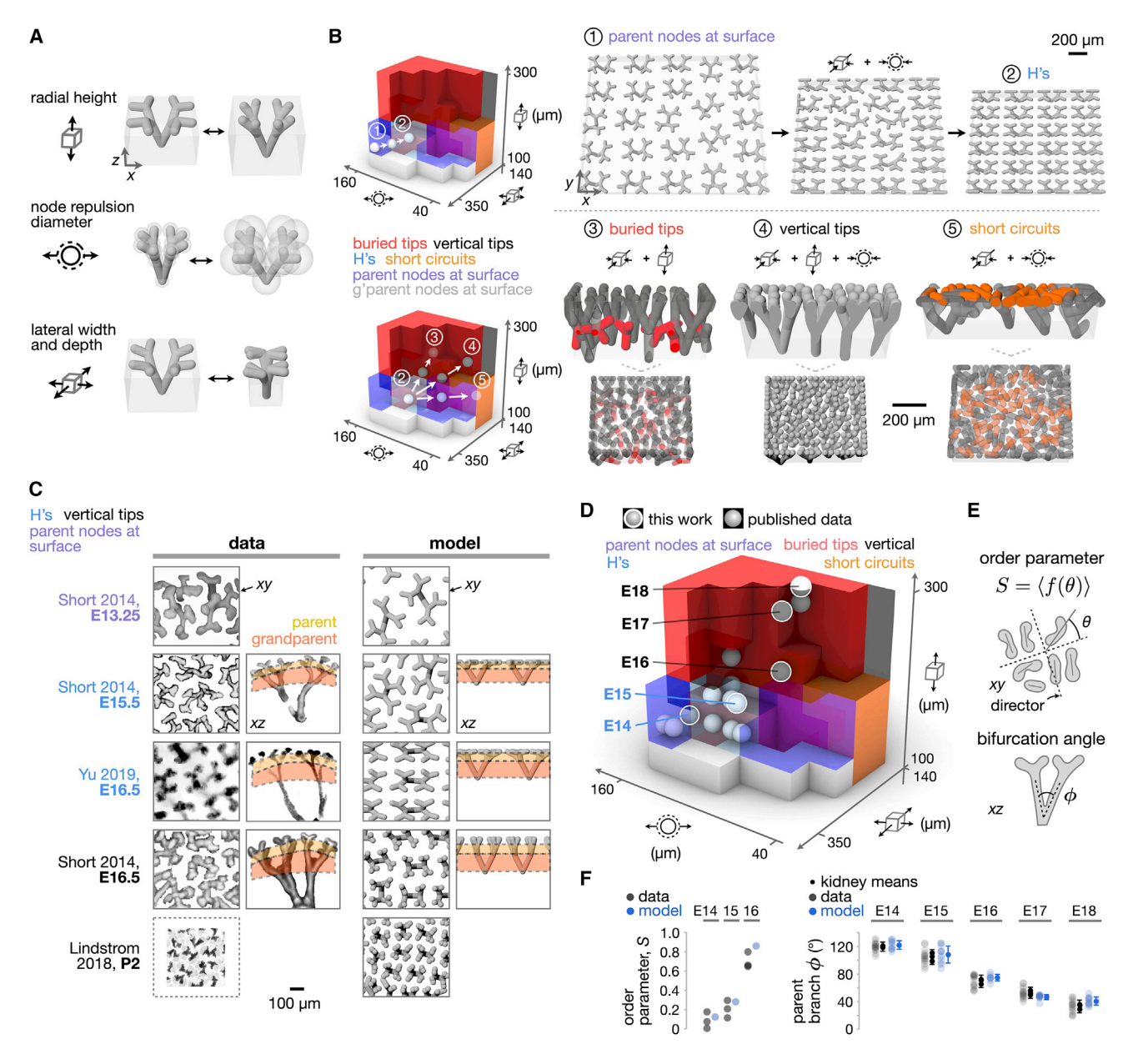


Figure 2. Published and measured kidney data map to a trajectory through physics-based model space that avoids defects (A) Model output demonstrating geometric parameters.

(B) Left, 3D plot of six geometric packing phases of tubule families within the model parameter space. Top row, an example trajectory from low tip density in the parent-nodes-at-surface phase into the H's phase. Bottom row, three possible trajectories from the H's phase into the buried tips, vertical, and short circuits phases. Insets show side views of model cases where red segments are buried in the model volume, and orange segments intersect with other segments. (C) Left, top and side views, where available, of published ureteric bud tubule tip patterns. Right, corresponding views from model cases with matching geometric parameters

- (D) Published kidneys and kidneys measured in this work (means of n = 3 kidneys per embryonic day) mapped to model phase space (see Figures S2 and S3 for full detail).
- (E) Quantitative metrics.

(F) Quantitation of metrics comparing kidneys from this work and model cases. Error bars at right are mean ± SD for all measurements pooled across n = 3 kidneys (technical replicates) for each embryonic day. All data are representative of two litters (biological replicates). Images of E13.25, E15.5, and E16.5 kidneys (lower panels) in (C) are reprinted from Short et al., ¹² Copyright (2014), with permission from Elsevier. Images of E16.5 kidneys (upper panels) are reprinted from Yu et al., ¹⁴ Copyright (2019), with permission from Elsevier. Images of P2 kidneys are used with permission from Lindström et al., ²⁰ Copyright (2018); permission conveyed through Copyright Clearance Center, Inc.

See also Figures S2 and S3 and Videos S1-S3.



Article

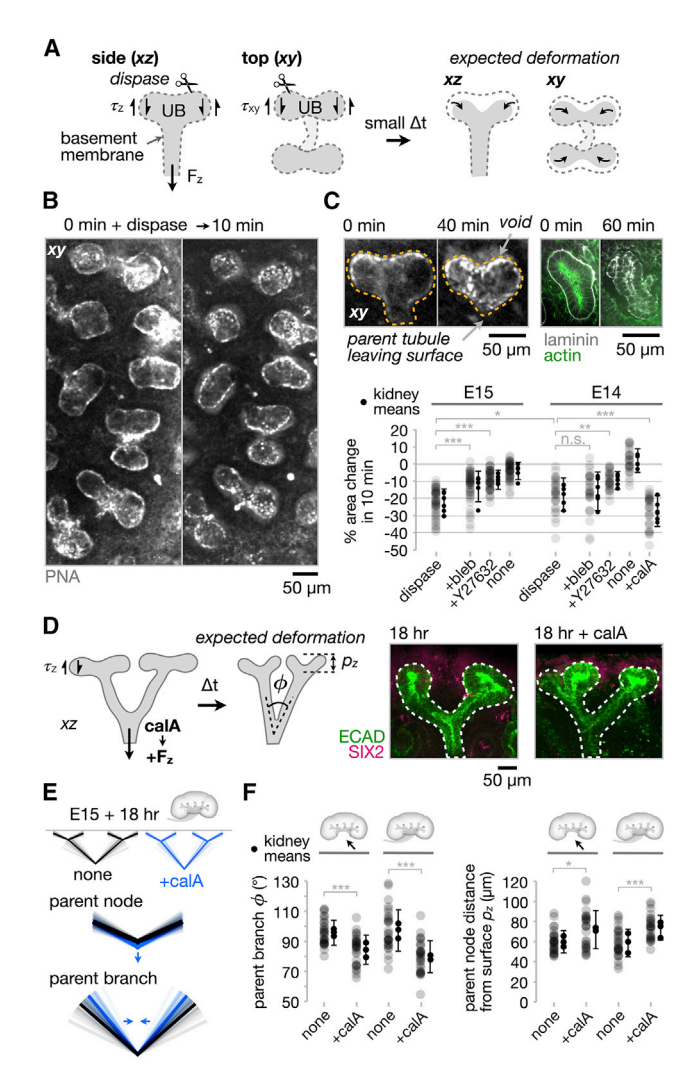


Figure 3. Radially oriented tubule tension is sufficient to promote a vertical packing transition

(A) Expected tubule family deformation after dispase treatment.

(B) Tip pattern in live E15 kidney explant before (left), and after 10 min dispase (right).

(C) Top left, example daughter tip pair. Top right, laminin (basement membrane) immunofluorescence for similar pairs \pm dispase. Bottom, tip area change after 10 min dispase; 60 min pre-treatment with 20 μM blebbistatin (bleb), 20 μM Y-27632, or 25 nM calyculin A (calA) followed by 10 min dispase; or no dispase (none) for E14 and E15 kidneys (>5 measurements per kidney, n = 6 kidneys per condition pooled from two biological replicates). Error bars are mean \pm SD across all measurements per condition.

(D) Left, expected tubule deformation following treatment with calA; φ = parent bifurcation angle, p_z = parent node distance from kidney surface. Right, control and calA-treated tubule families after 18 h culture.

(E) Pictographs of family deformation using φ and ρ_z data from (F). Transparent lines are individual measurements, solid lines are means.

(F) Quantitation of φ and p_z for kidneys \pm ureter, and \pm calA for 18 h (5 measurements per n = 3 kidneys per condition). Error bars are mean \pm SD across all measurements per condition.

(C and F) One-way ANOVA, Tukey's test (*p < 0.05, *p < 0.01, **p < 0.001). Individual kidneys represent technical replicates, all data are representative of two litters (biological replicates).

See also Figures S4A and S4B, Table S1, and Video S4.

great-grandparent nodes move further from the kidney surface (note increase in yellow and orange layer heights in Figure 2C). Nodes moving deeper into the kidney away from the surface would create a kind of swiveling effect of tubules, so that they move closer together and the angles between them would reduce. Lindström et al. described "node retraction" as retrograde movement of branch points toward the ureter beginning at ~E15,36 which is consistent with our data showing a reduction in parent branch bifurcation angle φ during the shift to vertical packing (Figures 2D and 2F; see also Short et al. 12). Short et al. also inferred from maps of branched trees that several branch generations are subsumed and contribute to the surface area of the renal pelvis as it expands. 12 This refined earlier observations²¹ and matches one expected consequence of Lindstrom's node retraction phenomenon. However, Lindstrom et al. did not determine if node retraction was caused by revision of branch point locations through collective cell dynamics or by an active force generated by the UB itself.

We reasoned that a radially oriented tension on tubule families (labeled F_z in Figure 3A, where z is the cartesian axis that points radially along the tubule family axis) could be indirectly measured by disrupting the basement membrane at the epithelial-mesenchymal interface. This would release adhesive and shear forces at that interface and cause tips and parent nodes to rapidly retract away from the kidney surface (Figure 3A). We disrupted this tissue interface using dispase, an enzyme that cleaves fibronectin and type IV collagen to preferentially dissociate basement membranes.³⁷ Dispase added to E15 kidney explants disrupted the basement membrane and caused epithelial delamination from the surrounding mesenchyme before tips and parent nodes retracted away from the kidney surface within 10 min (Figures 3B, 3C, and S4A; Video S4). Tracking the basal tubule surface through time-lapse imaging revealed that the UB retracts within the xz plane, whereas the mesenchyme remains relatively stationary (Figure S7), consistent with our hypothesis. We measured tip areas at the kidney surface as a proxy for retraction (Figures 3B and S4) and found that it decreased significantly relative to untreated controls (Figure 3C). This decrease was mitigated by pre-treatment with either the myosin II ATPase inhibitor blebbistatin (bleb) or the Rho-associated kinase (ROCK) inhibitor Y-27632 that inhibits contractility by reducing myosin II light-chain phosphorylation (Figure 3C). We repeated this analysis for kidneys at E14 to test whether tubule forces are reduced in the developmental period before node retraction and pelvis remodeling begin. E14 kidneys showed less tubule retraction following dispase treatment compared with E15 but returned to the retraction level of E15 kidneys in the presence of calyculin A (calA), which stimulates actomyosin contractility^{38,39} (Figure 3C). These data indicate that tubules at the epithelial-mesenchymal interface are subject to an actomyosin-based radial tension that builds between ~E14 and E15, as the shift to vertical packing begins.

Is this retraction force then sufficient to shift tubule families from the crystalline H's state to vertical packing? We hypothesized that increasing actomyosin-based contraction within the ureteric tree would drive vertical packing, as measured through a decrease in φ and an increase in the parent node distance from the kidney surface (p_z) (Figure 3D). To test this hypothesis, we treated intact E15 kidney explants with 25 nM calA in culture

Article



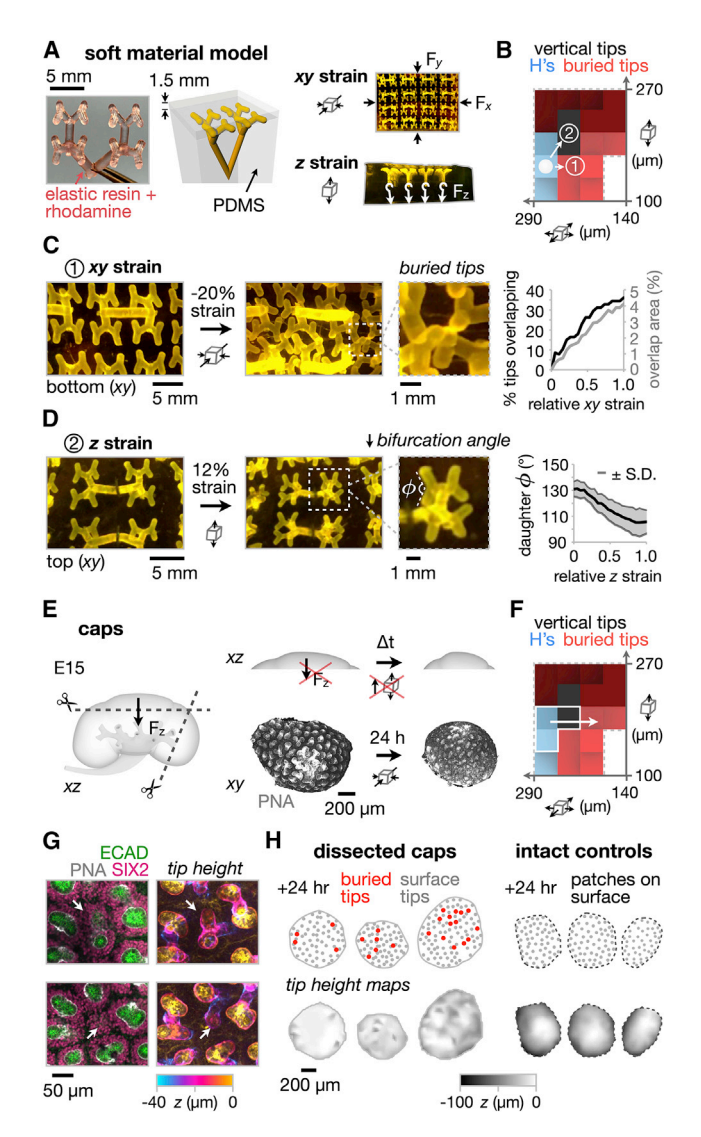


Figure 4. Radially oriented tubule tension is necessary to avoid buried tips

(A) Left, 3D-printed elastic tubule family. Middle, rendering of embedding in polydimethylsiloxane (PDMS) silicone. Right, top and side view of tubule family array and deformation modes.

(B) 2D section of phase space showing expected transitions under strain in xy and z

(C) Left, photographs of tubule positions taken from underside of the model before and after strain is applied in *xy*. Right, quantitation of tip overlap metrics. (D) Left, similar photographs for added strain in *z*. Right, quantitation of daughter branch bifurcation angle with ±SD envelope.

(E) Left and top, cartoon of cap dissection and change in strain parameters over time in culture. Bottom, confocal projections of a cap before and after 24-h culture.

(F) 2D section of phase space showing expected transition for caps in culture.
(G) Buried tips shown as left, confocal immunofluorescence image, right, depth-coded projection; one example per image row.

(H) Top, pictographs of surface and buried tip locations after 24 h culture. Bottom, tip height maps interpolated from (x,y,z) positions of tips. Buried tips measurements are collected from n=4 kidneys/caps (technical replicates). All data are representative of two litters (biological replicates). See also Figures S4C and S4D, Table S1, and Video S5.

for 18 h, followed by fixation, immunofluorescence staining, optical clearing, and confocal imaging of tubule families. Indeed, φ decreased and p_z increased in the calA-treated kidneys compared with untreated controls (Figures 3E and 3F). Similar data were also recovered from kidney explants for which the ureter was removed (Figures 3E and 3F), revealing that the radial tension mediating the transition to vertical packing does not originate within the upper ureter, but is either applied directly to tubule families by the adjacent stroma or is intrinsic to the UB during this rearrangement phase.

Tension on tubule families in the radial direction of the kidney is necessary to avoid buried tips

If the physical effects of geometric crowding, tip repulsion, and tubule tension are primarily responsible for tip positions, similar outcomes should translate to material systems with similar geometry but lacking biological dynamics. We 3D printed a model of ~E16 tubule families that share a great-great-grandparent node as elastic filaments, impregnated them with fluorescent rhodamine, and embedded them in arrays near the surface of a block of soft 50:1 (pre-polymer base:curing agent) polydimethylsiloxane (PDMS) silicone elastomer (Figure 4A; Video S5). Since the average distance between ureteric tubule tips decreases by <30% from E15.5 to postnatal day 2,20 the PDMS embedding medium mimics an approximately fixed repulsion distance between tips maintained by the mesenchyme and stroma, whereas the mechanical flexibility in each polymer allows tips to move in space and adopt energetically favorable positions and orientations. Applying up to -20% compressive strains in xy that mimic tip crowding by duplication were sufficient to create overlapping tip defects as some tips rotated and deflected downward away from the surface of the embedding medium (Figures 4B-4D). Second, applying up to 12% elongation strains in z were sufficient to create closer clustering of daughter branches and reduce the bifurcation angles between sisters, similar to the change in tubule morphology during the vertical tip transition. Although the mechanical properties of epithelial tubules and cap mesenchyme niches are poorly understood, our soft material modeling efforts here demonstrate that physical interactions among tips and their embedding medium in the presence of strains acting at long range are sufficient to explain buried and vertical tip patterning transitions.

Beyond interrogating the normal transition of tubule families to the vertical orientation in live kidney explants, we next saw an opportunity to test the simulation predictions by forcing a defective packing transition. One tractable strategy would be to eliminate F₇ from the UB tree during the onset of vertical packing (~E15-E16) by severing tubules (and removing force transmission) roughly below the great-grandparent nodes prior to culture (Figure 4E). Both the computational and soft material models predict that this would create buried rather than vertical tips near the kidney surface, assuming that decreases in the lateral xy domain size occupied by tubule families continues normally (Figure 4F). We therefore dissected caps of E15 kidney cortex and cultured them for 24 h. Caps compacted in xy area by $11\% \pm 6\%$ (n = 10 caps, Table S1) during this time, accentuating the normal lateral confinement of tubule families. In accordance with the computational and soft material models, we found that 34 of 290 tips were buried below the surface of dissected caps



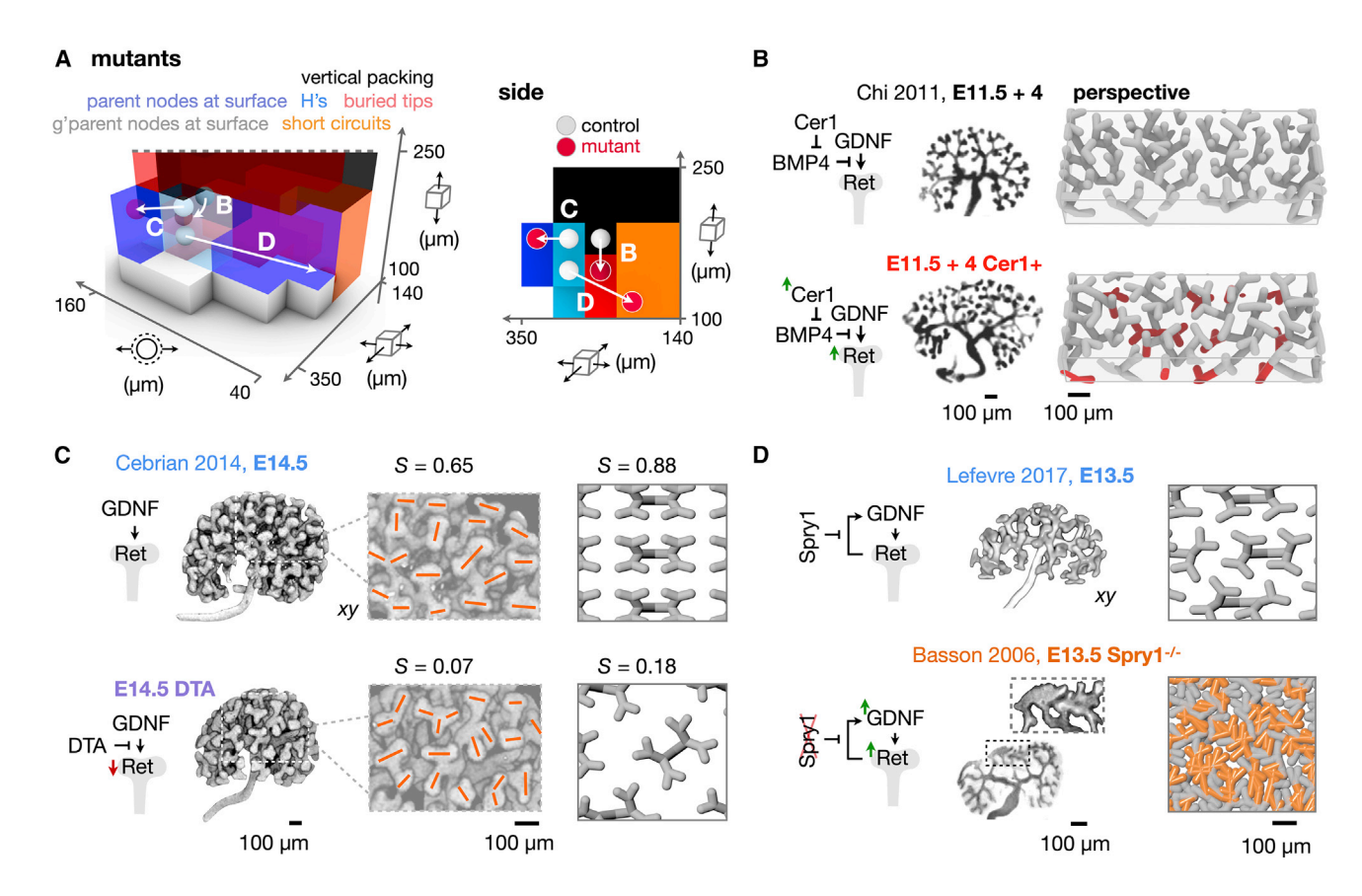


Figure 5. Published mutants map to conflicted or developmentally regressive model phases

(A) Left, a portion of the model phase diagram showing predicted packing phases based on geometric properties of normal control kidneys (white markers) compared with mutant kidneys in (B)-(D) (red markers). Right, side view projection of kidney data on relevant phases, more clearly showing predicted packing

(B) Left, cartoons of Cer1 interaction with the Gdnf/Ret pathway central to branching morphogenesis. Middle, fluorescence micrographs reproduced from Chi et al. for E11.5 kidneys cultured for 4 days. Right, model predictions of branch geometry in wild-type and Cer1+ mutant.

(C) Similar data for wild-type and diphtheria toxin A (DTA)-induced cap mesenchyme ablation in Cebrian et al. including annotations of tip orientation (orange) and

(D) Similar data for wild-type and Spry1^{-/-} kidneys. Images are from the indicated papers; model results are both based on measurements made from kidneys reported in Lefevre et al. Images of control and Cer1+ kidneys in (B) are adapted from Chi et al. 40 and are licensed under a Creative Commons Attribution License (CC BY 4.0). Images of control and DTA kidneys in (C) are reprinted from Cebrian et al., ⁴¹ Copyright (2014) with permission from Elsevier. Image of the control kidney in (D) is used with permission of The Company of Biologists, Ltd., Lefevre et al., ²³ Copyright (2017); permission conveyed through Copyright Clearance Center, Inc. Image of the Spry1^{-/-} kidney in (D) is reprinted from Basson et al., Copyright (2006) with permission from Elsevier.

after 24 h (across n = 4 caps), whereas none of a total of 463 were buried across controls consisting of intact kidneys (n = 4 kidneys), caps fixed immediately after cutting (n = 4 caps), and caps cultured for 24 h, although adhered to the substrate by their cut surface to limit lateral confinement of tubule families (n = 4 caps) (Figures 4G, 4H, S4B, and S4C; Table S1). Buried tips were visible as "dimples" in tip height maps for dissected caps after 24 h in culture, in contrast to smooth height maps for all controls (Figures 4H and S4C). This experiment revealed that radially oriented tension in tubule families are necessary for UB tubule families to resolve into vertical packing without generating buried tip defects.

Mouse mutants exhibit defective or regressive tubule packing phases

Finally, we wondered if our model could predict the impacts of developmental defects on UB organization. To do this, we quantitatively examined images of three published mouse mutant kidneys with altered branching phenotypes and mapped their spatial parameters to the model phase diagram (Figure 5A). Overexpression of the bone morphogenetic protein (BMP) family antagonist Cerberus 1 (Cer1+) induces ectopic "side branches" in the UB, which were also reported in kidney explants after air-liquid interface culture. 40 Indeed, although such culture conditions distort kidney dimensions and branch morphology, 17 when spatial variables of Cer1+ kidney tubule families were measured and plotted on the model phase diagram, they accurately placed this kidney in the buried tips phase at E11.5 + 4 days in culture. In comparison, wild-type kidneys mapped to the expected vertical packing phase under the same culture conditions (Figures 5A and 5B).

In a separate study, Cebrian et al. engineered a Gdnf^{Cre} mouse line to produce diphtheria toxin A (DTA) in Gdnf-expressing cap mesenchyme cells.41 DTA-exposure at E12.5 was sufficient to

Article



reduce the cap mesenchyme population by ~40% within 24 h and DTA-exposed kidneys continued to develop. However, these kidneys became hypoplastic, ultimately producing fewer nephrons at birth, despite retaining normal gross tubule organization.⁴¹ In this study, wild-type kidneys appeared to have typical daughter branch orientational order parameter (S) properties of an ~E15-E16 kidney, comparing against our own data and other publications. The corresponding E14.5 DTA-exposed kidney mapped to the parent-nodes-at-surface phase rather than the H's phase as for the wild-type age-matched control and showed a corresponding drop in S that was mirrored by model cases (Figures 5A and 5C). Rather than DTA-exposed kidneys simply having fewer tips in the same H's pattern as for the wild type, the mutant instead has fewer tips arranged in the more disordered (lower S) packing pattern predicted for an earlier developmental stage.

Finally, genetic knockout or knockdown of the GDNF/Ret antagonist Sprouty 1 (Spry1-/-) tends to produce kidneys with poorly spaced tubules that occasionally appear cystic, incompletely branched, or fused, with more frequent branching events and shorter tubule lengths between branch points. 7,23,42,43 Mapping the spatial variables of E13.5 Spry1^{-/-} mutants to the model space placed them in the short circuits phase rather than the H's phase as for stage-matched wild-type kidneys from the same study (Figures 5A and 5D). Intriguingly, although Cer1+ and Sprv1-/- mutations each reportedly increase GDNF/Ret signaling activity (Figures 5B and 5D), we found they mapped to different defective packing phases. This may be due to subtle differences in biological activity. Cer1 is a BMP antagonist, and since BMP family proteins are implicated in tip mutual repulsion. 16 altered tip repulsion mechanisms may drive Cer1+ mutants to the buried tips packing phase. This effect may be absent in the Spry1^{-/-} mutants, since loss of Spry1 appears to directly stimulate branching through increased Ret tyrosine kinase activity, creating regions of high local UB tip density^{7,42} that resemble the short circuits packing phase. Taken together, these pieces of evidence suggest that genetic perturbations can force tubule families to occupy defective or developmentally regressive packing phases in vivo, revealing that the model morphospace may provide insight into abnormal cell and tissue dynamics contributing to observed ureteric tree morphologies.

DISCUSSION

Here, we use physics-based simulations, soft material modeling, and kidney explants to reveal how the kidney negotiates a conflict between limited surface area and increasing tip number. Previous modeling approaches have for example considered mechanisms for branch formation based on cellular automata with local rules for cell behavior, 44 stochastic branching, and density-dependent tip termination 5 (which is less applicable to the kidney than other organs 10), Turing reaction-diffusion at early stages of ureteric branching, 46,47 deterministic rules that operate locally to tips or between them, 23,48 and tip spatial distribution based on geometric rules that are more agnostic to biological processes. 14,36 Our approach extends the latter to consider competition between UB epithelial branching and geometric constraints imposed by packing. One outcome of this tradeoff is the

emergence of a frustrated state of daughter-and-parent tubule units organized over long range at the kidney surface. This state is sensitive to transitions to defective packing phases and must be actively resolved by transitioning to vertical packing to accommodate branching after ~E16.

Our model and explant experiments show that UB tip organization is restricted to a narrow range of packing geometries and that tubule tension must be actively modulated to avoid defects. Our data do not account for other corrective behaviors that kidney tubules may adopt on the fly. For example, Lefevre et al. used spatial proximity and tubule lineage analysis to infer that tips mutually inhibit each other's bifurcation, but not their elongation. This would aid in preventing overcrowding and fusion or overlap of tips in the vertical tips phase by gradually bringing tip bifurcation to a halt. Indeed, several other UB, mesenchymal, basement membrane, and early nephron factors are thought to contribute to branch termination and maturation as morphogenesis halts.

The necessity for a retraction force on tubule families suggests several questions for further study. Where do the forces that promote node retraction originate? Static tension can be transmitted across epithelial tissues due to supracellular actomyosin contractility among polarized and adhered cells. 50,51 Tension could also result from cell intercalation (rearrangement) events that govern tubule convergent extension⁵² and/or cell collective migration.³⁶ which could be distinguished by live imaging. Finally, how is tension spatiotemporally coordinated between tubule families? Lindstrom et al. suggest that since node retraction is asynchronous between tubule families there is no global trigger for it, rather it would be caused by local epithelial-stromal communication.³⁶ Even so, is there a mechanistic link between pelvis formation and retraction force besides their temporal coincidence? One hypothesis is that the expanding pelvis could draw in lower branch generations, although also triggering retraction throughout the tubule network. This could occur, for example, through recently described mechanochemical feedback between collective epithelial cell polarization, EGFR/ERK activation, and contractile force. 53,54

Once tubule families reach the vertical packing phase, our model suggests that there are no other structural remodeling options for increasing tip surface density. If mouse kidneys are optimally packed, it would appear impossible for larger kidneys with more restrictive surface area:volume ratios to evolve. However, additional levels of hierarchical organization can overcome the geometric constraints imposed by packing nephrons into a single lobe (renicule) as in the mouse kidney. Human and bovine kidneys are composed of multiple lobes that all still share a border with the kidney surface, but which attach to a proportionally more extensive system of papillae and calyces that drain into the renal pelvis. 20,55 This would increase the surface area-tofunctional volume of the kidney to a point, at the expense of larger drainage networks. Cetaceans and other marine mammals exhibit yet another hierarchical shift-their kidneys contain closely packed renicules, each encapsulated and roughly the size of mouse kidneys, such that not all renicules occupy organ surface area, yet all individually retain cortico-medullary structure. 55,56 Thus, physical constraints may have exerted selective pressure on the morphology of tubule families and whole kidneys as mammals increased in size over evolutionary time.



In summary, we show that the developing UB encounters a physical packing problem that constrains surface tip distribution and number. Whether this ultimately limits nephron endowment in the adult organ is an intriguing focus for current and future study. ¹⁸ Furthermore, to avoid organizational issues that could further impair kidney function, the UB must actively restructure itself using actomyosin-based tensions to pull branch point nodes away from the surface, permitting increased tubule packing density. Finally, our work suggests new design guidelines for engineered renal tissues and new classification criteria for branching morphogenesis phenotypes, both in normal development and congenital kidney disease.

Limitations of the study

Our geometric model does not model UB branching and generates static predictions of tubule organization through energy minimization. UB branching is asynchronous, 12 whereas our model simulates an array of tubule families with identical initial geometry. Asynchronous branching and surface curvature may contribute to co-existence of phases in the same kidney35 but does not significantly affect our conclusions here. Our study is also limited to analysis of immediately fixed embryonic kidneys. Ideally, changes in packing phase over time could be live-imaged in real time, but current explant culture approaches rely on flattening the kidney at an air-liquid-interface or between two surfaces, 57-59 disrupting normal branching architecture. Experiments with dispase-treated live kidney explants (Figures 3A-3C) indicate that tubules are subject to an actomyosin-based force at ~E15, but we have not yet identified the collective cell mechanisms that produce this force, leaving an opportunity for future study. Further testing of specific hypotheses for how UB tip families transition between phases or the cellular basis of node retraction would benefit from advances in either intravital imaging or ex vivo culture.

STAR*METHODS

Detailed methods are provided in the online version of this paper and include the following:

- KEY RESOURCES TABLE
- RESOURCE AVAILABILITY
 - Lead contact
 - Materials availability
 - Data and code availability
- EXPERIMENTAL MODEL AND SUBJECT DETAILS
 - Animals and animal handling
- METHOD DETAILS
 - Kidney explant experiments
 - Immunofluorescence and optical clearing
 - Imaging
 - Tip packing models
 - Soft material model
 - Image analysis
- QUANTIFICATION AND STATISTICAL ANALYSIS

SUPPLEMENTAL INFORMATION

Supplemental information can be found online at https://doi.org/10.1016/j.

ACKNOWLEDGMENTS

We would like to thank Hughes lab members and the instructors and students of the 2021 MBL Embryology course for training, discussion, and advice. We are grateful to A. Gupta, K. Sasaki, and Y. Sakata for technical assistance with kidney dissections; to D. Piker for technical comments on the Kangaroo2 solver; and to L. Bugaj, A. Raj, and W. Marshall for feedback on the manuscript. This work was supported by: NIH F32 fellowship DK126385 (L.S.P.), the Predoctoral Training Program in Developmental Biology T32HD083185 (J.M.V.), NIH MIRA R35GM133380 (A.J.H.), and NSF CAREER award 2047271 (A.J.H.).

AUTHOR CONTRIBUTIONS

Conceptualization, L.S.P. and A.J.H.; methodology, L.S.P., J.M.V., J.L., and A.J.H.; software, A.J.H.; formal analysis, L.S.P. and A.J.H.; investigation, L.S.P., J.M.V., J.L., and A.J.H.; writing—original draft, L.S.P. and A.J.H.; writing—review and editing, L.S.P., J.M.V., J.L., and A.J.H.; visualization, L.S.P. and A.J.H.; supervision, L.S.P. and A.J.H.; project administration, A.J.H.

DECLARATION OF INTERESTS

The authors declare no competing interests.

INCLUSION AND DIVERSITY

The authors support inclusive, diverse, and equitable conduct of research.

Received: April 15, 2022 Revised: October 17, 2022 Accepted: December 20, 2022 Published: January 23, 2023

REFERENCES

- 1. Smith, J.M. (1978). Optimization theory in evolution. Annu. Rev. Ecol. Syst.
- Mauroy, B., Filoche, M., Weibel, E.R., and Sapoval, B. (2004). An optimal bronchial tree may be dangerous. Nature 427, 633–636. https://doi.org/ 10.1038/nature02287.
- Diamond, J.M. (1992). Evolutionary physiology. The red flag of optimality. Nature 355, 204–206. https://doi.org/10.1038/355204a0.
- Costantini, F., and Kopan, R. (2010). Patterning a complex organ: branching morphogenesis and nephron segmentation in kidney development. Dev. Cell 18, 698–712. https://doi.org/10.1016/j.devcel.2010.04.008.
- Smyth, I.M. (2021). Development of the metanephric kidney. Curr. Top. Dev. Biol. 143, 111–150. https://doi.org/10.1016/bs.ctdb.2020.09.003.
- Little, M.H., and McMahon, A.P. (2012). Mammalian kidney development: principles, progress, and projections. Cold Spring Harb. Perspect. Biol. 4, a008300. https://doi.org/10.1101/cshperspect.a008300.
- Basson, M.A., Watson-Johnson, J., Shakya, R., Akbulut, S., Hyink, D., Costantini, F.D., Wilson, P.D., Mason, I.J., and Licht, J.D. (2006). Branching morphogenesis of the ureteric epithelium during kidney development is coordinated by the opposing functions of GDNF and Sprouty1. Dev. Biol. 299, 466–477. https://doi.org/10.1016/j.ydbio.2006.08.051.
- Durbec, P., Marcos-Gutierrez, C.V., Kilkenny, C., Grigoriou, M., Wartiowaara, K., Suvanto, P., Smith, D., Ponder, B., Costantini, F., and Saarma, M. (1996). GDNF signalling through the Ret receptor tyrosine kinase. Nature 381, 789–793. https://doi.org/10.1038/381789a0.
- Sainio, K., Suvanto, P., Davies, J., Wartiovaara, J., Wartiovaara, K., Saarma, M., Arumäe, U., Meng, X., Lindahl, M., Pachnis, V., et al. (1997). Glial-cell-line-derived neurotrophic factor is required for bud initiation from ureteric epithelium. Development 124, 4077–4087. https://doi. org/10.1242/dev.124.20.4077.
- Short, K.M., Combes, A.N., Lisnyak, V., Lefevre, J.G., Jones, L.K., Little, M.H., Hamilton, N.A., and Smyth, I.M. (2018). Branching morphogenesis in the developing kidney is not impacted by nephron formation or integration. eLife 7, e38992. https://doi.org/10.7554/eLife.38992.

Article



- 11. Carroll, T.J., Park, J.-S., Hayashi, S., Majumdar, A., and McMahon, A.P. (2005). Wnt9b plays a central role in the regulation of mesenchymal to epithelial transitions underlying organogenesis of the mammalian urogenital system. Dev. Cell 9, 283-292. https://doi.org/10.1016/j.devcel.2005. 05.016.
- 12. Short, K.M., Combes, A.N., Lefevre, J., Ju, A.L., Georgas, K.M., Lamberton, T., Cairncross, O., Rumballe, B.A., McMahon, A.P., Hamilton, N.A., et al. (2014). Global quantification of tissue dynamics in the developing mouse kidney. Dev. Cell 29, 188-202. https://doi.org/10. 1016/j.devcel.2014.02.017.
- 13. Rumballe, B.A., Georgas, K.M., Combes, A.N., Ju, A.L., Gilbert, T., and Little, M.H. (2011). Nephron formation adopts a novel spatial topology at cessation of nephrogenesis. Dev. Biol. 360, 110-122. https://doi.org/10. 1016/j.ydbio.2011.09.011.
- 14. Yu, W., Marshall, W.F., Metzger, R.J., Brakeman, P.R., Morsut, L., Lim, W., and Mostov, K.E. (2019). Simple rules determine distinct patterns of branching morphogenesis. Cell Syst. 9, 221-227. https://doi.org/10. 1016/j.cels.2019.08.001.
- 15. Metzger, R.J., Klein, O.D., Martin, G.R., and Krasnow, M.A. (2008). The branching programme of mouse lung development. Nature 453, 745-750. https://doi.org/10.1038/nature07005.
- 16. Davies, J.A., Hohenstein, P., Chang, C.-H., and Berry, R. (2014). A selfavoidance mechanism in patterning of the urinary collecting duct tree. BMC Dev. Biol. 14, 35. https://doi.org/10.1186/s12861-014-0035-8.
- 17. Combes, A.N., Lefevre, J.G., Wilson, S., Hamilton, N.A., and Little, M.H. (2016). Cap mesenchyme cell swarming during kidney development is influenced by attraction, repulsion, and adhesion to the ureteric tip. Dev. Biol. 418, 297-306. https://doi.org/10.1016/j.ydbio.2016.06.028.
- 18. Viola, J.M., Liu, J., Prahl, L.S., Huang, A., Chan, T.J., Hayward-Lara, G., Porter, C.M., Shi, C., Zhang, J., and Hughes, A.J. (2022). Tubule jamming in the developing kidney creates cyclical mechanical stresses instructive to in vitro nephron formation. Preprint at bioRxiv. https://doi.org/10. 1101/2022.06.03.494718.
- 19. Combes, A.N., Short, K.M., Lefevre, J., Hamilton, N.A., Little, M.H., and Smyth, I.M. (2014). An integrated pipeline for the multidimensional analysis of branching morphogenesis. Nat. Protoc. 9, 2859-2879. https://doi.org/ 10.1038/nprot.2014.193.
- 20. Lindström, N.O., McMahon, J.A., Guo, J., Tran, T., Guo, Q., Rutledge, E., Parvez, R.K., Saribekyan, G., Schuler, R.E., Liao, C., et al. (2018). Conserved and divergent features of Human and mouse kidney organogenesis. J. Am. Soc. Nephrol. 29, 785-805. https://doi.org/10.1681/ ASN.2017080887.
- 21. Osathanondh, V., and Potter, E.L. (1963). Development of human kidney as shown by microdissection. II. Renal pelvis, calyces, and papillae. Arch. Pathol. 76, 277-289.
- 22. Sampogna, R.V., Schneider, L., and Al-Awgati, Q. (2015). Developmental programming of branching morphogenesis in the kidney. J. Am. Soc. Nephrol. 26, 2414-2422. https://doi.org/10.1681/ASN.2014090886.
- 23. Lefevre, J.G., Short, K.M., Lamberton, T.O., Michos, O., Graf, D., Smyth, I.M., and Hamilton, N.A. (2017). Branching morphogenesis in the developing kidney is governed by rules that pattern the ureteric tree. Development 144, 4377-4385. https://doi.org/10.1242/dev.153874.
- 24. Shah, M.M., Sampogna, R.V., Sakurai, H., Bush, K.T., and Nigam, S.K. (2004). Branching morphogenesis and kidney disease. Development 131, 1449-1462. https://doi.org/10.1242/dev.01089.
- 25. Moritz, K.M., Singh, R.R., Probyn, M.E., and Denton, K.M. (2009). Developmental programming of a reduced nephron endowment: more than just a baby's birth weight. Am. J. Physiol. Ren. Physiol. 296, F1-F9. https://doi.org/10.1152/ajprenal.00049.2008.
- 26. Luyckx, V.A., Bertram, J.F., Brenner, B.M., Fall, C., Hoy, W.E., Ozanne, S.E., and Vikse, B.E. (2013). Effect of fetal and child health on kidney development and long-term risk of hypertension and kidney disease. Lancet 382, 273-283. https://doi.org/10.1016/S0140-6736(13)60311-6.

- 27. Elmore, S.A., Kavari, S.L., Hoenerhoff, M.J., Mahler, B., Scott, B.E., Yabe, K., and Seely, J.C. (2019). Histology atlas of the developing mouse urinary system with emphasis on prenatal days E10.5-E18.5. Toxicol. Pathol. 47, 865-886. https://doi.org/10.1177/0192623319873871.
- 28. Yao, Z. (2020). Stress-induced ordering of two-dimensional packings of elastic spheres. Phys. Rev. E 101, 062904. https://doi.org/10.1103/ PhysRevE.101.062904.
- 29. Zu, M., Tan, P., and Xu, N. (2017). Forming quasicrystals by monodisperse soft core particles. Nat. Commun. 8, 2089. https://doi.org/10.1038/ s41467-017-02316-3.
- 30. Miller, W.L., and Cacciuto, A. (2011). Two-dimensional packing of soft particles and the soft generalized Thomson problem. Soft Matter 7, 7552-7559. https://doi.org/10.1039/C1SM05731F.
- 31. Goldberg, M. (1970). The packing of equal circles in a square. Math. Mag. 43, 24-30. https://doi.org/10.1080/0025570X.1970.11975991.
- 32. Zhang, Q., Li, J., Nijjer, J., Lu, H., Kothari, M., Alert, R., Cohen, T., and Yan, J. (2021). Morphogenesis and cell ordering in confined bacterial biofilms. Proc. Natl. Acad. Sci. USA 118. https://doi.org/10.1073/pnas. 2107107118.
- 33. Bausch, A.R., Bowick, M.J., Cacciuto, A., Dinsmore, A.D., Hsu, M.F., Nelson, D.R., Nikolaides, M.G., Travesset, A., and Weitz, D.A. (2003). Grain boundary scars and spherical crystallography. Science 5, 299.
- 34. Kroner, E., and Anthony, K.H. (1975). Dislocations and disclinations in material structures: the basic topological concepts. Annu. Rev. Mater. Sci. 5, 43-72. https://doi.org/10.1146/annurev.ms.05.080175.000355.
- 35. Viola, J.M., Liu, J., Prahl, L.S., Huang, A., Chan, T.J., Hayward-Lara, G., Porter, C.M., and Hughes, A.J. (2022). Tubule jamming in the developing kidney creates cyclical mechanical stresses instructive to in vitro nephron formation. Preprint at bioRxiv. https://doi.org/10.1101/2022.06. 03.494718.
- 36. Lindström, N.O., Chang, C.-H., Valerius, M.T., Hohenstein, P., and Davies, J.A. (2015). Node retraction during patterning of the urinary collecting duct system. J. Anat. 226, 13-21. https://doi.org/10.1111/joa.12239.
- 37. Stenn, K.S., Link, R., Moellmann, G., Madri, J., and Kuklinska, E. (1989). Dispase, a neutral protease from Bacillus polymyxa, is a powerful fibronectinase and type IV collagenase. J. Invest. Dermatol. 93, 287-290. https://doi.org/10.1111/1523-1747.ep12277593.
- 38. Shver, A.E., Rodrigues, A.R., Schroeder, G.G., Kassianidou, E., Kumar, S., and Harland, R.M. (2017). Emergent cellular self-organization and mechanosensation initiate follicle pattern in the avian skin. Science 357, 811–815. https://doi.org/10.1126/science.aai7868.
- 39. Chartier, L., Rankin, L.L., Allen, R.E., Kato, Y., Fusetani, N., Karaki, H., Watabe, S., and Hartshorne, D.J. (1991). Calyculin-A increases the level of protein phosphorylation and changes the shape of 3T3 fibroblasts. Cell Motil. Cytoskeleton 18, 26-40. https://doi.org/10.1002/cm. 970180104
- 40. Chi, L., Saarela, U., Railo, A., Prunskaite-Hyyryläinen, R., Skovorodkin, I., Anthony, S., Katsu, K., Liu, Y., Shan, J., Salgueiro, A.M., et al. (2011). A secreted BMP antagonist, Cer1, fine tunes the spatial organization of the ureteric bud tree during mouse kidney development. PLoS One 6, e27676. https://doi.org/10.1371/journal.pone.0027676.
- 41. Cebrian, C., Asai, N., D'Agati, V., and Costantini, F. (2014). The number of fetal nephron progenitor cells limits ureteric branching and adult nephron endowment. Cell Rep. 7, 127-137. https://doi.org/10.1016/j.celrep.2014.
- 42. Basson, M.A., Akbulut, S., Watson-Johnson, J., Simon, R., Carroll, T.J., Shakya, R., Gross, I., Martin, G.R., Lufkin, T., McMahon, A.P., et al. (2005). Sprouty1 is a critical regulator of GDNF/RET-mediated kidney induction. Dev. Cell 8, 229-239. https://doi.org/10.1016/j.devcel.2004. 12.004.
- 43. Gross, I., Morrison, D.J., Hyink, D.P., Georgas, K., English, M.A., Mericskay, M., Hosono, S., Sassoon, D., Wilson, P.D., Little, M., et al. (2003). The receptor tyrosine kinase regulator Sprouty1 is a target of the



- tumor suppressor WT1 and important for kidney development. J. Biol. Chem. 278, 41420–41430. https://doi.org/10.1074/jbc.M306425200.
- Lambert, B., MacLean, A.L., Fletcher, A.G., Combes, A.N., Little, M.H., and Byrne, H.M. (2018). Bayesian inference of agent-based models: a tool for studying kidney branching morphogenesis. J. Math. Biol. 76, 1673–1697. https://doi.org/10.1007/s00285-018-1208-z.
- Hannezo, E., Scheele, C.L.G.J., Moad, M., Drogo, N., Heer, R., Sampogna, R.V., van Rheenen, J., and Simons, B.D. (2017). A unifying theory of branching morphogenesis. Cell 171, 242–255.e27. https://doi.org/ 10.1016/j.cell.2017.08.026.
- Menshykau, D., Michos, O., Lang, C., Conrad, L., McMahon, A.P., and Iber, D. (2019). Image-based modeling of kidney branching morphogenesis reveals GDNF-RET based Turing-type mechanism and patternmodulating WNT11 feedback. Nat. Commun. 10, 239. https://doi.org/10. 1038/s41467-018-08212-8.
- Turing, A.M. (1952). The chemical basis of morphogenesis. Phil. Trans. R. Soc. Lond. B 237, 37–72. https://doi.org/10.1098/rstb.1952.0012.
- Zubkov, V.S., Combes, A.N., Short, K.M., Lefevre, J., Hamilton, N.A., Smyth, I.M., Little, M.H., and Byrne, H.M. (2015). A spatially-averaged mathematical model of kidney branching morphogenesis. J. Theor. Biol. 379, 24–37. https://doi.org/10.1016/j.jtbi.2015.04.015.
- Nigam, S.K., and Shah, M.M. (2009). How does the ureteric bud branch?
 J. Am. Soc. Nephrol. 20, 1465–1469. https://doi.org/10.1681/ASN. 2008020132
- Legoff, L., Rouault, H., and Lecuit, T. (2013). A global pattern of mechanical stress polarizes cell divisions and cell shape in the growing Drosophila wing disc. Development 140, 4051–4059. https://doi.org/10.1242/dev.090878.
- Vasquez, C.G., and Martin, A.C. (2016). Force transmission in epithelial tissues. Dev. Dyn. 245, 361–371. https://doi.org/10.1002/dvdy.24384.
- Karner, C.M., Chirumamilla, R., Aoki, S., Igarashi, P., Wallingford, J.B., and Carroll, T.J. (2009). Wnt9b signaling regulates planar cell polarity and kidney tubule morphogenesis. Nat. Genet. 41, 793–799. https://doi.org/10. 1038/ng.400.
- Hino, N., Rossetti, L., Marín-Llauradó, A., Aoki, K., Trepat, X., Matsuda, M., and Hirashima, T. (2020). ERK-mediated mechanochemical waves direct collective cell polarization. Dev. Cell 53, 646–660.e8. https://doi.org/10. 1016/j.devcel.2020.05.011.
- Aoki, K., Kondo, Y., Naoki, H., Hiratsuka, T., Itoh, R.E., and Matsuda, M. (2017). Propagating wave of ERK activation orients collective cell migration. Dev. Cell 43, 305–317.e5. https://doi.org/10.1016/j.devcel.2017. 10.016.
- Little, M.H. (2021). Returning to kidney development to deliver synthetic kidneys. Dev. Biol. 474, 22–36. https://doi.org/10.1016/j.ydbio.2020. 12.009.
- Maluf, N.S.R., and Gassman, J.J. (1998). Kidneys of the Killerwhale and significance of Reniculism. Anat. Rec. 250, 34–44. https://doi.org/10. 1002/(SICI)1097-0185(199801)250:1<34::AID-AR4>3.0.CO;2-E.
- Sebinger, D.D.R., Unbekandt, M., Ganeva, V.V., Ofenbauer, A., Werner, C., and Davies, J.A. (2010). A novel, low-volume method for organ culture of embryonic kidneys that allows development of cortico-medullary anatomical organization. PLoS One 5, e10550. https://doi.org/10.1371/ journal.pone.0010550.

- Saarela, U., Akram, S.U., Desgrange, A., Rak-Raszewska, A., Shan, J., Cereghini, S., Ronkainen, V.P., Heikkilä, J., Skovorodkin, I., and Vainio, S.J. (2017). Novel fixed z-direction (FiZD) kidney primordia and an organoid culture system for time-lapse confocal imaging. Development 144, 1113–1117. https://doi.org/10.1242/dev.142950.
- Lawlor, K.T., Zappia, L., Lefevre, J., Park, J.S., Hamilton, N.A., Oshlack, A., Little, M.H., and Combes, A.N. (2019). Nephron progenitor commitment is a stochastic process influenced by cell migration. eLife 8, e41156. https://doi.org/10.7554/eLife.41156.
- Schindelin, J., Arganda-Carreras, I., Frise, E., Kaynig, V., Longair, M., Pietzsch, T., Preibisch, S., Rueden, C., Saalfeld, S., Schmid, B., et al. (2012). Fiji: an open-source platform for biological-image analysis. Nat. Methods 9, 676–682. https://doi.org/10.1038/nmeth.2019.
- Wanek, N., Muneoka, K., Holler-Dinsmore, G., Burton, R., and Bryant, S.V. (1989). A staging system for mouse limb development. J. Exp. Zool. 249, 41–49. https://doi.org/10.1002/jez.1402490109.
- Figard, L., and Sokac, A.M. (2011). Imaging cell shape change in living Drosophila embryos. J. Vis. Exp. 49, 2503.
- 63. O'Brien, L.L., Combes, A.N., Short, K.M., Lindström, N.O., Whitney, P.H., Cullen-McEwen, L.A., Ju, A., Abdelhalim, A., Michos, O., Bertram, J.F., et al. (2018). Wnt11 directs nephron progenitor polarity and motile behavior ultimately determining nephron endowment. eLife 7, e40392. https://doi.org/10.7554/eLife.40392.
- 64. Hama, H., Kurokawa, H., Kawano, H., Ando, R., Shimogori, T., Noda, H., Fukami, K., Sakaue-Sawano, A., and Miyawaki, A. (2011). Scale: a chemical approach for fluorescence imaging and reconstruction of transparent mouse brain. Nat. Neurosci. 14, 1481–1488. https://doi.org/10.1038/nn.2928.
- Cuvilliers, P., Yang, J.R., Coar, L., and Mueller, C. (2018). A comparison of two algorithms for the simulation of bending-active structures. Int. J. Space Struct. 33, 73–85. https://doi.org/10.1177/0266351118779979.
- Bouaziz, S., Martin, S., Liu, T., Kavan, L., and Pauly, M. (2014). Projective dynamics: fusing constraint projections for fast simulation. ACM Trans. Graph. 33, 1–11. https://doi.org/10.1145/2601097.2601116.
- Barnes, M.R. (1999). Form finding and analysis of tension structures by dynamic relaxation. Int. J. Space Struct. 14, 89–104. https://doi.org/10.1260/0266351991494722.
- Miki, M., Adriaenssens, S., Igarashi, T., and Kawaguchi, K. (2014). The geodesic dynamic relaxation method for problems of equilibrium with equality constraint conditions. Int. J. Numer. Methods Eng. 99, 682–710. https://doi.org/10.1002/nme.4713.
- Tinevez, J.-Y., Perry, N., Schindelin, J., Hoopes, G.M., Reynolds, G.D., Laplantine, E., Bednarek, S.Y., Shorte, S.L., and Eliceiri, K.W. (2017). TrackMate: an open and extensible platform for single-particle tracking. Methods 115, 80–90. https://doi.org/10.1016/j.ymeth.2016.09.016.
- Morales-Navarrete, H., Nonaka, H., Scholich, A., Segovia-Miranda, F., de Back, W., Meyer, K., Bogorad, R.L., Koteliansky, V., Brusch, L., Kalaidzidis, Y., et al. (2019). Liquid-crystal organization of liver tissue. eLife 8, e44860. https://doi.org/10.7554/eLife.44860.
- Mercurieva, A.A., and Birshtein, T.M. (1992). Liquid-crystalline ordering in two-dimensional systems with discrete symmetry. Makromol. Chem. Theory Simul. 1, 205–214. https://doi.org/10.1002/mats.1992.040010402.
- de Gennes, P.G., and Prost, J. (1993). The Physics of Liquid Crystals (Clarendon Press).

Developmental Cell Article



STAR***METHODS**

KEY RESOURCES TABLE

REAGENT or RESOURCE	SOURCE	IDENTIFIER
Antibodies		
Mouse monoclonal anti-calbindin D-28K, clone CB-955	Sigma	Cat#C9849; RRID: AB_476894
Mouse monoclonal anti-E-cadherin, clone 34	BD Biosciences	Cat#610404; RRID: AB_397787
Rabbit polyclonal anti-laminin	Abcam	Cat#ab11575; RRID: AB_298179
Rabbit polyclonal anti-SIX2	Proteintech	Cat #11562-1-AP; RRID: AB_2189084
Rat monoclonal anti-CD140a/PDGFRA	eBioscience	Cat#14-1401-82; RRID: AB_467491
Donkey anti-rabbit Alexa Fluor 647	ThermoFisher	Cat#A-31573; RRID: AB_2536183
Donkey anti-rabbit Alexa Fluor 555	ThermoFisher	Cat#A-31570; RRID: AB_2536180
Donkey anti-mouse Alexa Fluor 555	ThermoFisher	Cat#A-31572; RRID: AB_162543
Donkey anti-rat Alexa Fluor 405	ThermoFisher	Cat#A48268; RRID: AB_2890549
Chemicals, peptides, and recombinant proteins		
Alexa Fluor 647 phalloidin	ThermoFisher	Cat#A22287
Calyculin A	Cell Signaling Technology	CAS:101932-71-2; Cat#9902S
Dispase	Corning	Cat# 354235
Lectin PNA from <i>Arachis hypogaea</i> (peanut), AlexaFluor 488 conjugate	ThermoFisher	Cat#L21409
Methacryloxyethyl thiocarbamoyl rhodamine B	Polysciences	CAS:669775-30-8; Cat#23591
(S)-(-)-Blebbistatin	Tocris	CAS:856925-71-8; Cat#1852
Y-27632 hydrochloride	STEMCELL Technologies	CAS:129830-38-2; Cat#72302
Deposited data		
Analysis codes	This paper; Mendeley Data	https://data.mendeley.com/datasets/ w6zfwfn8hj/1
Rhino Grasshopper 3D model file	This paper; Mendeley Data	https://data.mendeley.com/datasets/ w6zfwfn8hj/1
Experimental models: Organisms/strains		
Mouse: Crl:CD1(ICR)	Charles River Laboratories	RRID:IMSR_CRL:022
Software and algorithms	·	
FIJI/ImageJ	Schindelin et al. ⁶⁰	https://imagej.nih.gov/ij/
Rhino Grasshopper 3D	Robert McNeel & Associates	https://www.rhino3d.com
Kangaroo2 Physics	Daniel Piker (Foster and Partners)	https://www.food4rhino.com/en/app/kangaroo-physics
Kangaroo2 solver goals	Daniel Piker (Foster and Partners)	https://github.com/Dan-Piker/K2Goals
Other		
Form3+ low force stereolithography 3D printer	FormLabs	PKG-F3-WSVC-BASIC
Elastic 50A resin	FormLabs	RS-F2-ELCL-01
1# (4 x 7.5 mm) fishing hooks	N/A	N/A
Nylon monofilament line	N/A	N/A
Sylgard 184 silicone elastomer	Ellsworth Adhesives	2065622

RESOURCE AVAILABILITY

Lead contact

Further information and requests for resources and reagents should be directed to and will be fulfilled by the lead contact, Alex Hughes (ajhughes@seas.upenn.edu).





Materials availability

This study did not generate new unique reagents.

Data and code availability

- Microscopy data reported in this paper will be shared by the lead contact upon request.
- All original code has been deposited in Mendeley Data and is publicly available as of the date of publication. DOIs are listed in the key resources table.
- Any additional information required to reanalyze the data reported in this paper is available from the lead contact upon request.

EXPERIMENTAL MODEL AND SUBJECT DETAILS

Animals and animal handling

All mouse experiments followed National Institutes of Health (NIH) guidelines and were approved by the Institutional Animal Care and Use Committee (IACUC) of the University of Pennsylvania (protocol number 807000). Embryos were collected from outbred wild-type timed pregnant CD-1 mice (Charles River Laboratories) at developmental stages between E14 and E18. Mice were housed in single-occupancy standard ventilated cages in a conventional rodent facility with free access to water and food and a 12 hour light cycle and were euthanized by CO2 inhalation. Developmental kidney stages were roughly confirmed by limb staging of whole embryos, as previously described. 12,61

METHOD DETAILS

Kidney explant experiments

Embryonic kidneys were dissected in chilled Dulbecco's phosphate buffered saline (DPBS, MT21-31-CV, Corning). For live explant experiments, kidneys were labeled with 20 μ g ml⁻¹ AlexaFluor 488-labeled peanut (*Arachis hypogaea*) agglutinin lectin (PNA, L21409, Sigma) in Dulbecco's minimum essential medium (DMEM, 10-013-CV, Corning) for 60 min and washed in 2 exchanges of DMEM. For dispase experiments, whole E14-E15 kidneys were incubated in DMEM containing PNA lectin and drugs for 60 min, washed with media and transferred to 2 mm-diameter wells to reduce sample movement during dispase addition. These wells were created with a biopsy punch in a ~5 mm-thick layer of 15:1 (base:crosslinker) PDMS elastomer (Sylgard 184, 2065622, Ellsworth Adhesives) set in 35 mm coverslip-bottom dishes (FD35-100, World Precision Instruments). A 1:1 mix of 50 U ml⁻¹ dispase (354235, Corning): DMEM was added immediately prior to time-lapse imaging. For cap experiments, E15 kidneys were further dissected using a razor blade to retrieve lateral border and superior pole tissue segments (Figure 4E). Kidneys and caps were labeled with PNA lectin and cultured for 24 hr at 37°C, 5% CO₂ in microplate wells coated with 1% agarose prior to fixing, immunostaining, and confocal imaging. As a control for tissue contraction, we secured dissected and lectin-labeled caps to an 18 mm x 18 mm coverslip using heptane glue ⁶² and cultured them in DMEM for 24 hours before fixing and immunostaining. Heptane glue was prepared by incubating double sided scotch tape (3M Corporation) in n-heptane (1043651000, Sigma) at room temperature overnight.

Drugs used in explant experiments include phosphatase inhibitor calyculin A (calA, 25 nM, 9902S, Cell Signaling Technology), myosin II ATPase inhibitor (S)-(-)-blebbistatin (blebb, 20 μΜ, 1852, Tocris Bioscience), or ROCK inhibitor Y-27632 hydrochloride (20 μM, 72304, STEMCELL Technologies). Calyculin A and blebbistatin were diluted in dimethyl sulfoxide (DMSO, D2650, Sigma) and stored in working aliquots (10 μM and 30 mM, respectively) at -20°C. Y-27632 was diluted in sterile DPBS at 10 mM and stored in working aliquots at -20°C. For dispase experiments, calA, blebb, and Y-27632 were diluted in PNA lectin labeling media immediately prior to use. PNA lectin was diluted to a 5 mg ml⁻¹ stock in DI water and stored in working aliquots at -20°C.

Immunofluorescence and optical clearing

Whole-mount immunofluorescence staining of whole kidneys and dissected cap explants was adapted from Combes et al. and O'Brien et al. 19,63 Dissected kidneys were fixed with ice cold 4% paraformaldehyde (PFA, 16% stock, 15710, Electron Microscopy Sciences) diluted in DPBS for 13-17 min or further processed for live analysis. Fixation time in PFA depended on the embryo stage, as previously described. 19 In some experiments, whole embryos were fixed overnight in 4% PFA at 4°C prior to dissection. PFA-fixed kidneys were washed three times (5 min each) in ice cold DPBS, blocked for 2 hr at room temperature in PBSTX (DPBS + 0.1% Triton X-100) containing 5% donkey serum (D9663, Sigma), and then incubated in primary followed by secondary antibodies in the same blocking buffer for at least 48 hr at 4°C, alternating with 3 washes in PBSTX totaling 12-24 hours at 4°C. Minimum duration of primary and secondary incubations and washes depended on the embryonic day of the embryos at dissection. ¹⁹ The E14 whole kidney image in Figures 1A and 1B and all kidneys used to measure parent branch angles and node distances from the kidney surface in Figures 2 and 3 were cleared for 2 days in ScaleA2 (4M urea + 0.1% Triton X-100 + 10% glycerol), followed by 2 days in ScaleB4 (8M urea + 0.1% Triton X-100)⁶⁴ and were imaged in 35 mm culture dishes or 24-well glass bottom plates containing ScaleA2. Tissue clearing by ScaleA2/B4 caused a 33 ± 6% increase in overall kidney cross sectional area (Table S1), which are similar to previously reported tissue expansion measurements using this clearing method.⁶⁴

Primary antibodies and dilutions included rabbit anti-Six2 (1:600, 11562-1-AP, Proteintech, RRID: AB_2189084), mouse anti-E-cadherin (clone 34, 1:200, 610404, BD Biosciences, RRID: AB_397787), mouse anti-calbindin D-28K (clone CB-955, 1:100,

Article



C9849, Sigma, RRID: AB_476894) rat anti-CD140/PDGFRA (1:200, 14-1401-82, eBioscience, RRID: AB_467491), and rabbit anti-laminin (1:50, ab11575, Abcam, RRID: 298179). Secondary antibodies (all raised in donkey) include anti-rabbit AlexaFluor 647 (1:300, A-31573, ThermoFisher, RRID: AB_2536183), anti-rabbit AlexaFluor 555 (1:300, A-31570, ThermoFisher, RRID: AB_2536180), anti-mouse AlexaFluor 555 (1:300, A-31572, ThermoFisher, RRID: AB_162543), and anti-rat AlexaFluor 405 (1:300, A48268, ThermoFisher). In some experiments, samples were counterstained with DAPI (300 nM, 4',6-diamidino-2-phenylindole; D1306, ThermoFisher), PNA lectin-Alexa 488 (20 μ g ml⁻¹), and/or AlexaFluor 647 phalloidin (1:40, A22287, ThermoFisher) diluted in blocking buffer for 2 hours at 4°C.

Imaging

Live and fixed kidney imaging was performed using a Nikon Ti2-E microscope equipped with a CSU-W1 spinning disk (Yokogawa), a white light LED, laser illumination (100 mW 405, 488, and 561 nm lasers and a 75 mW 640 nm laser), a Prime 95B back-illuminated sCMOS camera (Photometrics), motorized stage, 4x/0.2 NA, 10x/0.25 NA and 20x/0.5 NA lenses (Nikon), and a stagetop environmental enclosure (OkoLabs). In dispase treatment experiments, a 150 μ m stack (21 frames, 7.5 μ m step size) of the kidney cortex was collected at each stage position every 5 minutes. Z-stacks of fixed and stained dispase-treated kidneys or cut caps (and controls) were similarly collected using 5 μ m step size (100-200 μ m, 21-41 frames) using either the 10x or 20x lens. In order to image the cortical kidney surface, caps were oriented cortex-side down against the glass surface of 35 mm dishes while uncut controls were oriented cortex-side down in the bottom of 2 mm-diameter PDMS wells, created as described above. The soft material model was imaged by submerging it in a transparent glass water bath and filming through an amber trans-illuminator filter (IO Rodeo) during manual manipulations under blue 470 nm LED illumination (ThorLabs M470L2-C1) using an iPhone 8 video camera.

Tip packing models

Tip packing simulations were performed using Kangaroo2 (Daniel Piker), a position-based dynamics solver within the Rhino Grasshopper algorithmic modeling environment (Robert McNeel & Associates). Kangaroo2 is used in architectural engineering to solve form-finding and structural problems subject to complex deformations, such as bending-active structures. ⁶⁵ We took a form-finding finite element approach here to enable rapid local solution to the packing problem for a 6 x 4 array of tubule families each sharing a great-grandparent node confined to a rectangular cuboid representing the surrounding kidney tissue (Figure S3; Video S2). The Kangaroo2 solver first defines geometric objects via their *xyz* coordinates using a point-based mesh, then applies forces to object vertices, which are combined in a weighted averaging step before incrementing the simulation time. ⁶⁶ After initial setup, the simulation algorithm iteratively moves points towards static equilibrium through dynamic relaxation. ⁶⁷ Solver goals are geometric conditions placed upon the entire simulation environment or specific structures. Each additional goal added to the system constitutes an energy term that is proportional to the squared distance between the current position of the affected structure and the 'target' position of the solver goal (see below for descriptions of specific goals). The solver algorithm seeks to minimize the sum of energy potentials associated with various simulation goals, allowing the system to transiently explore local energy minima as it converges towards equilibrium. The solver also employs a drift damping algorithm to minimize overshooting and oscillations, where drift damping is a combination of viscous and kinetic damping whose value changes between acceleration and deceleration. ⁶⁸

Solver goals used in our simulation include the Load, Length, SphereCollide, SolidPointCollide, and AnchorXYZ goals. Each of these define projection vectors that act upon a set of points to guide them towards a specific geometric goal. User-customizable, open source code describing Kangaroo2 solver goals is available at (https://github.com/Dan-Piker/K2Goals). The goals used in the current model are as follows:

- Load represents a point load, with a given magnitude V and vector direction \mathbf{u} in (x,y,z).
- Length defines a rest length between two points, where deviations (either compressive or tensile) behave as an elastic spring with stiffness K.
- SphereCollide defines an elastic spring with a rest length equal to the summed radii of an interacting pair of spheres $(r_1 + r_2)$ and stiffness K when $r < r_1 + r_2$, where r is the separation distance between centroids. When $r > r_1 + r_2$, forces are set to zero.
- SolidPointCollide checks whether a given point in mesh **M** is inside a nearby mesh **M**' and moves its (x,y,z) coordinates to the nearest point in **M**'.
- AnchorXYZ defines the projection of a given point or set of points (x, y, z) onto a plane and sets the point (if anchored in 1 axis) or
 plane (if anchored in 2 axes) as the target.

A detailed schematic of initial conditions, phase diagram construction, and model output is provided in Figure S2B. Tubule families were constructed from nodes and edges at a scale of $85 \mu m$ per model unit. Daughter, parent, and grandparent tubule lengths show little temporal variation across E13.5-E16.5 and were set at 57, 73, and 120 μm respectively for all model cases to roughly match those in the mouse kidney. Model parameters were given relative energy potential weightings called 'strengths'. All edges were modeled as linear elastic elements with an arbitrarily high strength of K = 100 and rest lengths equal to their initial lengths. Nodes were repulsive with strength R = 0.8 and diameter D. Nodes received a vertical load toward the model kidney surface of strength V = 0.5. Strengths controlling node repulsion from the cuboid boundaries and anchoring great-grandparent nodes to the lower boundary were both set arbitrarily high at 100 and 1000 respectively. R = 0.8 and V = 0.8 parameters are not readily measurable from kidney



samples, instead they were manually adjusted to qualitatively fit the models to tubule families' bifurcation angles in E16.5 kidney data from Yu et al. and then fixed for all other simulations.¹⁴

The model phase diagram was constructed by sweeping through an 'input space' (defined by xy extent of the confining cuboid, z extent of the cuboid, and repulsion diameter D) and assigning a phase to the output at each set of input variables (see below). The phase diagram is then plotted for linear ranges in the input variables (Figure S2B), however, the axes shown throughout the paper are in terms of 'output space' variables: 1) the square root of the area of tubule families at the cortical surface (~lateral width and depth of confinement, xy'), 2) the radial height of tubule families (z'), and 3) the apparent repulsion distance between tip centers (D'). Relationships between the values of input space and output space variables for all simulation cases not falling in the inefficiently packed phase are shown in Figure S5. The parameter sweep ranges were approximately centered around the H's phase and increments in each axis were chosen to keep the number of parameter sets to a reasonable number for manual assignment of phases. The parameter limits were chosen to capture model behavior in the neighborhood of the data from kidney examples. Other areas of the phase diagram give tubule packings that are generally distant from the observed biology, for example, any part of the phase space for xy' > 350 gives tip patterns that are inefficiently (i.e. not close) packed (shown in Figure S3B).

Phases were assigned by semi-quantitative assessment of tip patterns in each of the 216 simulations. Namely, grandparent and parent nodes at surface cases were indicated for simulations in which >90% of grandparent and parent nodes were at the model surface, respectively. H's were a subset of parent nodes at surface cases in which daughter orientational order parameter S > 0.5, indicating the 'Zu Sun' orientation described in Yu et al. 14 Buried tips cases were indicated when >10% of tips were buried beneath the model surface. Vertical tips cases were indicated when <10% of parent nodes were at the model surface. Short circuits cases were indicated when >10% of branches spatially overlapped. Inefficient packing cases were indicated when at least one gap of size > D appeared between neighboring tubule families in the model output. While the position of any given tip was dependent on initial conditions, the phase assignments were not, since the same phases were recorded in all cases when starting from the solution of the previous variable set as for starting with a reset model. Tubule families from experiments and literature were mapped to the model input space by measuring the three output variables (xy', z', and D') averaged across at least 3 tubule families per kidney, finding the nearest simulation case having the smallest sum of squared error across the three variables, and plotting in terms of the input variable values for that case. Kidney data fit to the model was then determined via orthogonal parameters to those used for mapping data to the model space, namely order parameters (see below) and branch bifurcation angles (Figure 2F).

Soft material model

Tubule families sharing great-great-grandparent nodes were modeled in Rhino to approximately match their dimensions in kidney trees from Yu et al. at E16.5.14 Models were scaled up isotropically by a factor of 30 to meet minimum resolution requirements for subsequent 3D printing in elastic resin (50A Shore durometer hardness, 3.23 MPa ultimate tensile strength) using a Form 3 printer (FormLabs). Tubule models were impregnated with 10 μM methacryloxyethyl thiocarbamoyl rhodamine B (Polysciences 23591) in acetone for 10 min, washed with DI water and dried for 1 hr at room temperature. The models were then placed in a 4 x 4 array on a 1.5 mm layer of 50:1 (pre-polymer base:curing agent) PDMS, degassed under vacuum, and cured in a 8 x 8 x 3.5 cm plastic container at 60°C for 2 hours. A second layer of degassed 50:1 PDMS was then poured until great-great-grandparent nodes were just exposed above the PDMS surface, and was then cured at 60°C overnight. 1# (4 x 7.5 mm) fishing hooks pre-tied with nylon monofilament line were secured to each great-great-grandparent node, and a final 50:1 PDMS layer was poured for a total model height of 3 cm. Nylon lines were held vertically over great-great-grandparent nodes during curing at 60°C overnight before demoulding the completed model from the plastic container.

Image analysis

Image annotations and measurements were performed in Fiji/ImageJ. 60 Tip domains and SIX2+ cap areas (Figure 1) were manually segmented using the polygon sections tool from confocal sections at the kidney surface, which we define as the xy plane. Residual area was calculated as the difference between the summed tip domain area and summed cap area for each image. Cap mesenchyme circularity values were calculated in FIJI from cap polygons according to circularity = $4\pi(A/P^2)$ where A is polygon area and P is polygon perimeter. Parent branch bifurcation angles (φ) and node distances from the kidney surface (p_z) (Figures 2 and 3) were manually annotated using Fiji/ImageJ's angle tool and line segment tool, respectively, from xz sections of cleared kidney data and model renderings. Soft material model strains, tip overlap, and tip angles (Figure 4) were similarly measured. Tubule tips at the kidney surface in dispase experiments (Figure 3) were also outlined by manually tracing the outline of PNA lectin signal using the polygon sections tool. Percentage area change was defined using the difference in recorded areas between the t = 0 and t = 10 min timepoints. We used a similar procedure to quantify kidney or cap area change due to cutting, calA treatment, ureter removal, or swelling from exposure to tissue clearing solvents (Table S1). Tip heights in whole kidneys and caps (Figure 4) were manually annotated by marking (x,y,z) coordinates at the center of tip lumens using the multi-point tool. Coordinates were translated into height maps using cubic interpolation via in-house MATLAB code (version R2020a, TheMathWorks Inc.). We used the FIJI TrackMate plugin⁶⁹ to manually track the movement of fluorescent PNA lectin puncta in the epithelium and mesenchyme from xy and xz confocal projections following dispase treatment (Figures S4A and S4B).





For orientation analysis of whole kidneys and the geometric model (Figure 2), we made use of order parameter metrics previously applied to liquid crystals^{70–72}:

For a 2D crystal :
$$S = \langle 2 \cos^2(\theta - \theta_d) - 1 \rangle$$
 (Equation 1)

Where θ is the orientation of an object and θ_d is the orientation of the 'nematic director', or the apparent preferred orientation of objects in a local field of view that serves as a reference axis. However, this metric cannot be directly applied. Since bifurcations are asynchronous, some new daughter branches are approximately orthogonal to nearby branches that have not yet bifurcated. This implies that the degree of order in daughter orientations should relate to their alignment along either orthogonal director. Histograms of daughter branch angles in the xy plane manually annotated in Fiji/ImageJ showed their overall orientations to be bimodal, with modes $\sim 90^{\circ}$ apart, such that directors for order parameter quantitation could be defined as the center of each mode. We therefore modified the 2D expression for S by adding a factor of 2 to the argument of $\cos^2(\theta)$, allowing S to quantify alignment along two orthogonal directors. Our orientational order parameter for daughter branches was therefore:

$$S = \langle 2\cos^2(2(\theta - \theta_{Mo})) - 1 \rangle$$
 (Equation 2)

Where θ are daughter branch angles and θ_{Mo} is the orientation of one of the directors ($\theta, \theta_{Mo} \in [0,180]$). This order parameter will therefore be S = 0 for random orientation of daughters, and S = 1 for perfect alignment of each daughter along either director.

QUANTIFICATION AND STATISTICAL ANALYSIS

All statistical analyses were performed in MATLAB and are described in figure legends. Unpaired t-tests (Welch's test) were used to make comparisons between two groups. One-way ANOVA and Tukey's post hoc test was used to compare multiple groups with n noted in legend. We determined statistical significance using a p < 0.05 cutoff. All error bars represent mean \pm standard deviation (s.d.) across all measurements. All data are representative of kidneys collected from at least two litters (independent biological replicates).